

DESIGN, MODELING AND OPTIMIZATION OF THE UNIVERSAL-SPATIAL ROBOTIC TAIL

William Rone

Robotics and Mechatronics Laboratory
Department of Mechanical Engineering
Virginia Tech
Blacksburg, VA, USA

Wael Saab

Robotics and Mechatronics Laboratory
Department of Mechanical Engineering
Virginia Tech
Blacksburg, VA, USA

Pinhas Ben-Tzvi

Robotics and Mechatronics Laboratory
Department of Mechanical Engineering
Virginia Tech
Blacksburg, VA, USA

ABSTRACT

This paper presents a novel robotic tail design that utilizes a serial chain of universal joints to generate spatial motion. In nature, animals utilize their tails to assist in maneuvering and stabilization while moving; this research aims to provide a robotic platform capable of extending these functionalities to a mobile robot. By utilizing a tail to assist in stabilization and maneuvering, the required functionality of other locomotion mechanisms in a mobile robot, such as legs, is reduced. The tail mechanism presented is actuated by sets of three cables routed along the robotic structure; quasi-independent segments within the tail are created by tying off a set of three cables to a link along the tail. Actuation is distributed within the underactuated mechanism by compression and extension springs mounted along the tail. Kinematic and dynamic analysis of the tail is performed to model the tail trajectory and predict the actuation requirements. Three methods of optimizing spring stiffnesses are provided that weigh different performance goals, and a methodology for using these results to select spring stiffnesses is provided. Results are generated to compare the kinematic, static and dynamic models to one another to analyze the impact the different loading effects have on the tail behavior.

1 INTRODUCTION AND BACKGROUND

A rich source of inspiration for robotics research in recent years has been bioinspired legged locomotion. However, the predominant focus on humanoid bipedal locomotion and leg-focused approaches (design/task-planning/control) for stabilization and maneuvering ignore the prevalence of tail-like structures in nature to assist in these functionalities.

The goal for including a tail-like structure on-board a mobile robot is to assist in the system's propulsion, maneuvering, stabilization and/or manipulation. This could be used to help augment an existing robot's functionality, or to offset the functionality required of another locomotion

mechanism. For example, in a legged robot, the tail could be used to help turn the system while walking or running [1] and to balance the robot in response to an external disturbance. This would allow the legs to primarily serve as a means of propulsion within the system, reducing their required complexity.

Previous research into robotic tails has primarily focused on single-degree of freedom pendulum-like structures that provide a single functionality, such as propulsion [2], stabilization [3] or maneuvering [4]. Examples of multi-functional tails presented in the literature include propulsion/maneuvering [5] and maneuvering/self-righting [6]. However, in order to justify the inclusion of a robotic tail on-board a legged robot, it should be capable of both reducing the required complexity in the legs and significantly enhancing functionality.

In addition, hyperredundant robotic structures more closely resemble tails observed in nature than simple pendulums. Two subsets of this class of robots are continuum and serpentine robots [7]. Continuum robots are defined by the continuous deformation of the robotic structure, instead of discrete displacements at defined joints [8]. These structures are primarily utilized on the meso-scale for medical procedures [9], although macro-scale manipulators have also been demonstrated [10]. Serpentine robots are typically composed of several identical rigid-link modules. These structures approximate continuous deformation with their serial chain of similar, compact links. These structures are primarily used as snake-like mobile robots [11], but have also been demonstrated as robotic manipulators [12].

A key challenge in adapting hyperredundant structures for use as a robotic tail is the need for cantilevered mounting of dynamic robotic structures. Previous macro-scale hyperredundant robots have either been high stiffness [13], which limits dynamic performance, or designed to be vertically

mounted [14], in which the structure hangs to reduce the moment induced by gravity in the joints. The significant effect of the tail's mass acting over relatively large distances from the base tends to cause large amount of 'sag' in elastic structures, or requires significant actuation to support it.

When considering the actuation of hyperredundant robots, two key challenges arise: (1) how to apply loading along the length of the structure, and (2) how to distribute that loading between redundant joints. In terms of challenge (1), a common approach is to utilize cable-driven actuation. The key benefit of cable-driven actuation is the ability to localize actuators at the base of the robot, reducing the minimum mass and size of the tail structure.

In terms of distributing actuation, two fundamental approaches may be considered: rigid, kinematic coupling or flexible, mechanical coupling. Rigid, kinematic coupling explicitly reduces the number of DOF of a hyperredundant mechanism by constraining the relative motion of adjacent joints, using structures such as gears or four-bar mechanisms. Flexible, mechanical coupling maintains the distinct DOF in various joints, but provides a means to re-distribute loading between links using elastic springs.

This paper focuses on a novel design approach for a robotic tail utilizing the second approach to distributing actuation (flexible, mechanical coupling; prior work has explored rigid, kinematic coupling [15,16]). It refines and extends the design concept and model presented in [17] to consider dynamics and spatial motion. The resulting design is called the Universal-Spatial Robotic Tail (USRT)—universal for its use of universal joints between links and spatial for its inherent spatial workspace. Section 2 details the design concept and dynamics model for the USRT. Section 3 presents methods of optimizing spring stiffness along the tail structure. Section 4 utilizes simulation results from these models to analyze tail performance. Section 5 summarizes the research and discusses planned future work, including experimental validation and joint-consideration of the tail with a legged robotic platform.

2 MECHANICAL DESIGN & DYNAMICS MODEL

This section presents the mechanical design concept for the universal-spatial robotic tail (USRT) and details the derivation

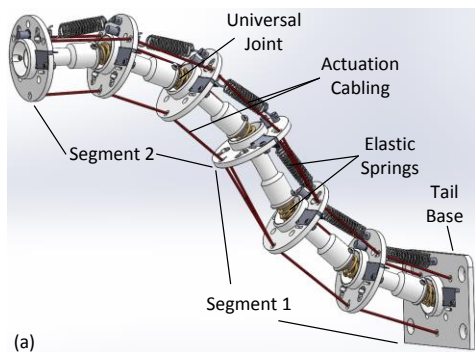


Figure 1. Universal-Spatial Robotic Tail (USRT).

of the design's dynamic model.

2.1 Design Concept

Figure 1 shows the USRT design concept. Six disks are serially connected from a base link through universal joints to allow relative pitch and yaw rotations between the disks while constraining relative roll. Each joint subsegment is designed with a joint stop to limit net bending in any given direction to a fixed angle. The tail is subdivided into two quasi-independent segments by six cables routed along its length. Three cables tie off at disk 3, and three cables tie off at disk 6.

The six cables are controlled by six motors. During operation, two of these cables will be tensioned, and the third will passively 'follow' the tail trajectory to maintain a negligible tension. This allows switching between which subset of two cables are tensioned during operation.

Actuation is distributed along the tail by elastic springs. As shown in Fig. 2, two types of springs are utilized: compression and extension. A compression spring is mounted around each universal joint to resist displacement from the straight configuration. The primary function of this spring is to distribute angular displacement when bending horizontally (i.e., yaw angles). An extension spring is mounted vertically above the compression spring in each subsegment and compensates for the induced moment due to gravity in the universal joint.

2.2 Dynamics Model

The tail's dynamics model will have 4 control inputs and 16 state variables. The 4 inputs are cable displacements: two for a pair of cables tying off at disk 3, and two for a pair of cables tying off at disk 6. These cable displacements will typically be the cables that are also in tension, but this is not a requirement. The 16 states are the 12 joint angles and the 4 cable tensions. The 12 joint angles correspond to the six pitch angles and six yaw angles that define the configurations of the six universal joints. The four cable tensions correspond to two positive tensions applied on cables at the base for each segment.

In order to calculate the trajectories of these 16 states, 16 governing equations are needed. Twelve of these equations come from joint equilibrium—a property of revolute joints is that they cannot support a moment aligned with their axis of

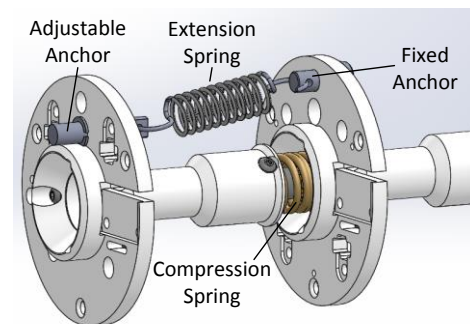


Figure 2. USRT subsegment with compression and extension elastic springs.

rotation. Given that a universal joint is composed of two orthogonal revolute joints, these governing equations can be calculated using Eq. 1, where ρ_i and γ_i define the joint i pitch- and yaw-axis unit vectors, respectively, and $M_{i,jnt}$ defines the net joint i moment at the universal joint center. As shown in Eq. 2, four loading effects will be included in $M_{i,jnt}$ for the dynamic model: inertia ($M_{i,inv}$), gravity ($M_{i,grv}$), universal-joint spring-dampener-actuator (USDA) ($M_{i,USDA}$) and cable ($M_{i,cbl}$); if $M_{i,inv}$ is neglected, the dynamic model becomes a static model.

$$\begin{cases} \rho_i^T M_{i,jnt} = 0, \\ \gamma_i^T M_{i,jnt} = 0 \end{cases} \quad i \in [1, \dots, 6] \quad (1)$$

$$M_{i,jnt} = M_{i,inv} - M_{i,grv} - M_{i,USDA} - M_{i,cbl} \quad (2)$$

The remaining four governing equations come from driving constraints that ensure the tail's joint angles generate cable routing paths that match the desired cable displacement. For cable j terminating in segment k , this condition is defined by Eq. 3, where $\delta_{j,k,des}$ and $\delta_{j,k}$ are the desired and calculated cable displacements.

$$\delta_{j,k} - \delta_{j,k,des} = 0 \quad (3)$$

This formulation of the mechanics model accounts for the two classes of loading along the tail—external and internal—in different ways. The external loading (gravity and inertia) depends on the sources of that loading ‘downstream’ of the joint under consideration. For example, joint 3 will account for the inertial loading and gravitational forces of disks 3-6. The internal loading (elasticity and cabling) accounts for forces and moments acting between two disks. Since the loading on adjacent disks is equal and opposite, the loading only affects the universal joint between those two disks.

2.2.1 Kinematic Analysis

Equation 4 defines the orientation matrices R_i of the disks from body 0 (the actuation module) to body 6, where I is the identity matrix; ϕ_i and θ_i are the universal joint i pitch- and yaw-joint angles, respectively; $R_y(\phi)$ is a y-axis rotation by angle ϕ ; and $R_x(\theta)$ is an x-axis rotation by angle θ . Using these rotation matrices, the joint axes ρ_i and γ_i may be defined using Eq. 5, where y_i^i and x_i^i are the i frame y- and x-axis unit vectors, respectively, defined in the i frame. By convention, in this analysis, a superscript denotes the frame in which a vector is defined; if a superscript is omitted, it is defined with respect to the ground frame.

$$R_i = \begin{cases} I & i = 0 \\ R_{i-1} R_i^{i-1} & i > 0 \end{cases}, \quad R_i^{i-1} = R_y(\phi_i) R_x(\theta_i) \quad (4)$$

$$\rho_i = R_{i-1} y_{i-1}^{i-1}, \quad \gamma_i = R_i x_i^i \quad (5)$$

For gravitational and inertial loading, the global-frame positions $p_{i,j,J2C}$ from joint i to the link j center-of-mass (COM) are required. To aid in this calculation, the joint positions $p_{i,jnt}$ and link COM positions $p_{i,COM}$ are calculated in Eqs. 6 and 7, where L_{J2J} is the distance between adjacent universal joint

centers, z_i^i is the i frame z-axis unit vector defined in the i frame, and L_{J2C} is the distance from joint i to the link i COM. Using these, $p_{i,j,J2C}$ is calculated using Eq. 8. These kinematic variables and others in the following analysis are illustrated in Fig. 3.

$$p_{i,jnt} = \begin{cases} \mathbf{0} & i = 1 \\ p_{i-1,jnt} + L_{J2J} R_{i-1} z_{i-1}^{i-1} & i > 1 \end{cases} \quad (6)$$

$$p_{i,COM} = p_{i,jnt} + L_{J2C} R_i z_i^i \quad (7)$$

$$p_{i,j,J2C} = p_{j,COM} - p_{i,jnt} \quad (8)$$

For both the USDA and cable loading in subsegment i , calculations require the relative position $p_{i,D2D}^{i-1}$ between the disk centers $i-1$ and i in the link $i-1$ frame. This is defined in Eq. 9, where $L_{D2J,0}$ is the distance from the disk 0 center (i.e., the centroid of the three cable routing holes in the actuation module) to joint 1, and L_{J2D} is the distance from joint i to the disk i center.

$$p_{i,D2D}^{i-1} = \begin{cases} L_{D2J,0} z_{i-1}^{i-1} + L_{J2D} R_{i-1} z_{i-1}^{i-1} & i = 1 \\ (L_{J2J} - L_{J2D}) z_{i-1}^{i-1} + L_{J2D} R_{i-1} z_{i-1}^{i-1} & i > 1 \end{cases} \quad (9)$$

For the USDA loading, the position vector $p_{i,spg}^{i-1}$ of the subsegment i extension spring and associated deformed spring length $L_{i,spg}$ are calculated using Eq. 10, where $p_{k,D2S}^i$ is the side k spring mounting position in the disk-frame and $\|a\|$ denotes the 2-norm of a . In addition, a vector $p_{i,J2S}$ from joint i to the subsegment i extension spring mount at disk i is defined in Eq. 11.

$$p_{i,spg}^{i-1} = -p_{1,D2S}^{i-1} + p_{i,D2D}^{i-1} + R_i^{i-1} p_{2,D2S}^i, \quad L_{i,spg} = \|p_{i,spg}^{i-1}\| \quad (10)$$

$$p_{i,J2S} = R_i (L_{J2D} z_i^i + p_{2,D2S}^i) \quad (11)$$

For actuation loading, the relative position $p_{i,j,H2H}^{i-1}$ of the

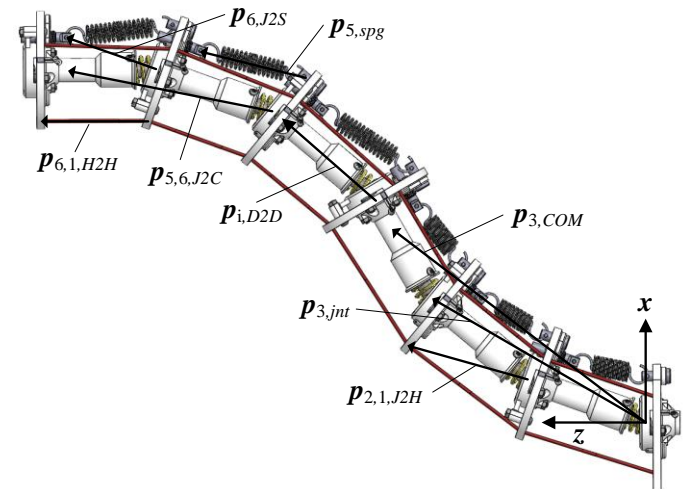


Figure 3. USRT subsegment with compression and extension elastic springs.

cable j routing holes between disks $i-1$ and i is defined in Eq. 12, where $\mathbf{p}_{j,hl}^i$ is the position vector from the disk i center to the disk i routing hole j defined in the disk-frame. This is used to calculate the segment k cable j displacement $\delta_{j,k}$ using Eq. 13, where $L_{H2H,0}$ is the distance between adjacent routing holes when the universal joint angles are zero. The position $\mathbf{p}_{i,j,2H}$ from joint i to the link i cable j routing hole is defined in Eq. 14.

$$\mathbf{p}_{i,j,H2H}^{i-1} = -\mathbf{p}_{j,hl}^{i-1} + \mathbf{p}_{i,D2D}^{i-1} + \mathbf{R}_i^{i-1} \mathbf{p}_{j,hl}^i \quad (12)$$

$$\delta_{j,k} = \sum_{i=1}^{3k} \left(\left\| \mathbf{p}_{i,j,H2H}^{i-1} \right\| - L_{H2H,0} \right) \quad (13)$$

$$\mathbf{p}_{i,j,2H} = \mathbf{R}_i \left(L_{J2D} \mathbf{z}_i^i + \mathbf{p}_{j,hl}^i \right) \quad (14)$$

The inertial loading also requires analysis of the tail's linear and angular velocities and accelerations. The links' angular velocities $\boldsymbol{\omega}_i$ are defined in Eq. 15, where \dot{x} denotes the first derivative with respect to time of x . The angular accelerations $\boldsymbol{\alpha}_i$, linear velocities $\mathbf{v}_{i,jnt}$ and $\mathbf{v}_{i,COM}$, and linear accelerations $\mathbf{a}_{i,jnt}$ and $\mathbf{a}_{i,COM}$ may be found by differentiating Eqs. 7, 8 and 15.

$$\boldsymbol{\omega}_i = \begin{cases} \mathbf{0} & i = 0 \\ \boldsymbol{\omega}_{i-1} + \mathbf{R}_{i-1} \boldsymbol{\omega}_{i-1,i}^{i-1} & i > 0 \end{cases}, \quad \boldsymbol{\omega}_{i-1,i}^{i-1} = \dot{\phi}_i \mathbf{y}_{i-1}^{i-1} + \dot{\theta}_i \mathbf{R}_i^{i-1} \mathbf{x}_i^i \quad (15)$$

2.2.2 Loading Analysis

The gravitational moment $\mathbf{M}_{i,grv}$ at joint i is due to the gravitational forces associated with disks i through 6. Equation 16 defines $\mathbf{M}_{i,grv}$, where m_j is the disk j mass, g is gravitational acceleration, \mathbf{x} is the global frame unit vector, and $\tilde{\mathbf{p}}\mathbf{F}$ denotes the cross product $\mathbf{p} \times \mathbf{F}$.

$$\mathbf{M}_{i,grv} = \sum_{j=i}^6 \tilde{\mathbf{p}}_{i,j,2C} \mathbf{F}_{j,grv}, \quad \mathbf{F}_{j,grv} = -m_j g \mathbf{x} \quad (16)$$

Like gravity, the inertia of links i through 6 will contribute to the joint i inertial moment. Equation 17 quantifies this relationship, where $\mathbf{F}_{j,inr,b}$ and $\mathbf{M}_{j,inr,b}$ are the body j inertial force and moment. They are defined in Eq. 18, where \mathbf{I}_j^j is the body-frame inertia tensor for link j .

$$\mathbf{M}_{i,inr} = \sum_{j=i}^6 \left(\mathbf{M}_{j,inr,b} + \tilde{\mathbf{p}}_{i,j,2C} \mathbf{F}_{j,inr,b} \right) \quad (17)$$

$$\mathbf{F}_{j,inr,b} = m_j \mathbf{a}_{j,COM}, \quad \mathbf{M}_{j,inr,b} = \mathbf{R}_j \mathbf{I}_j^j \mathbf{R}_j^T \boldsymbol{\alpha}_j + \tilde{\boldsymbol{\omega}}_j \mathbf{R}_j \mathbf{I}_j^j \mathbf{R}_j^T \boldsymbol{\omega}_j \quad (18)$$

The joint i USDA moment $\mathbf{M}_{i,USDA}$, defined in Eq. 19, represents the net moment acting at the joint due to four sources of loading in each subsegment: the extension spring ($\mathbf{M}_{i,ex}$), the compression spring ($\mathbf{M}_{i,cp}$), the joint dampening ($\mathbf{M}_{i,dmp}$) and the joint angle limit ($\mathbf{M}_{i,lim}$).

$$\mathbf{M}_{i,USDA} = \mathbf{M}_{i,ex} + \mathbf{M}_{i,cp} + \mathbf{M}_{i,dmp} + \mathbf{M}_{i,lim} \quad (19)$$

The subsegment i extension spring generates a force $\mathbf{F}_{i,spg}$ that contributes to $\mathbf{M}_{i,ex}$, defined in Eq. 20. $\mathbf{F}_{i,spg}$ is defined for the subsegment i extension spring in Eq. 21, where $k_{i,ex}$ is the spring stiffness, $L_{i,spg,0}$ is the unloaded spring length, $F_{i,spg,0}$ is the spring pretension and $\hat{\mathbf{p}}$ is the unit vector of \mathbf{p} , such that $\hat{\mathbf{p}} = \mathbf{p} / \|\mathbf{p}\|$.

$$\mathbf{M}_{i,ex} = \tilde{\mathbf{p}}_{i,J2S} \mathbf{F}_{i,spg} \quad (20)$$

$$\mathbf{F}_{i,spg} = -\left(k_{i,ex} (L_{i,spg} - L_{i,spg,0}) + F_{i,spg,0} \right) \mathbf{R}_{i-1} \hat{\mathbf{p}}_{i,spg}^{i-1} \quad (21)$$

The bending of the joint i compression spring generates a moment $\mathbf{M}_{i,cp}$ normal to the bending plane. The deflection magnitude $\beta_{i,jnt}$ is calculated using Eq. 22 as the angle between the link $i-1$ z-axis (\mathbf{z}_{i-1}^{i-1}) and the link i z-axis ($\mathbf{z}_i^{i-1} = \mathbf{R}_i^{i-1} \mathbf{z}_i^i$). The cross-product between these axes divided by the sine of $\beta_{i,jnt}$ defines the normal along which $\mathbf{M}_{i,cp}$ acts, leading to Eq. 23, where $k_{i,cp}$ is the bending stiffness. The small angle assumption is used to avoid the singularity when $\beta_{i,jnt} = 0$ —for less than 5° , $\sin \beta_{i,jnt} \approx \beta_{i,jnt}$. Given the definition of the normal, Eq. 22 is solved for a value of $\beta_{i,jnt}$ within the range $[0, \pi/2]$.

$$\beta_{i,jnt} = \text{acos} \left(\left(\mathbf{z}_{i-1}^{i-1} \right)^T \mathbf{R}_i^{i-1} \mathbf{z}_i^i \right) \quad (22)$$

$$\mathbf{M}_{i,cp} = \begin{cases} -k_{i,cp} \beta_{i,jnt} \mathbf{R}_{i-1} \left(\tilde{\mathbf{z}}_{i-1}^{i-1} \mathbf{R}_i^{i-1} \mathbf{z}_i^i \right) / \sin \beta_{i,jnt} & \beta_{i,jnt} > 5^\circ \\ -k_{i,cp} \mathbf{R}_{i-1} \left(\tilde{\mathbf{z}}_{i-1}^{i-1} \mathbf{R}_i^{i-1} \mathbf{z}_i^i \right) & \beta_{i,jnt} \leq 5^\circ \end{cases} \quad (23)$$

Several effects that lead to energy loss in the subsegment (spring deformation, contact friction at the joints, etc.), are lumped into a single dampening parameter dependent on the joint i bending velocity $\dot{\beta}_{i,jnt}$. This velocity is defined by the x- and y- components of $\boldsymbol{\omega}_{i-1,i}^{i-1}$ (defined in Eq. 15) by neglecting the z-component (which is associated with the link's roll velocity), as shown in Eq. 24. The resulting $\mathbf{M}_{i,dmp}$ is defined in Eq. 25 using $\boldsymbol{\omega}_{i-1,i,\hat{\beta}}^{i-1}$, where $c_{i,dmp}$ is the joint dampening parameter.

$$\dot{\beta}_{i,jnt} = \left\| \boldsymbol{\omega}_{i-1,i,\hat{\beta}}^{i-1} \right\|, \quad \boldsymbol{\omega}_{i-1,i,\hat{\beta}}^{i-1} = \left[\omega_{i-1,i,x}^{i-1} \quad \omega_{i-1,i,y}^{i-1} \quad 0 \right]^T \quad (24)$$

$$\mathbf{M}_{i,dmp} = -c_{i,dmp} \mathbf{R}_{i-1} \boldsymbol{\omega}_{i-1,i,\hat{\beta}}^{i-1} \quad (25)$$

The joint limiter will be modeled as a nonlinear spring-dampener that engages when $\beta_{i,jnt} > \beta_{lim}$. Equation 26 defines $\mathbf{M}_{i,lim}$, where $k_{i,lim}$ and $c_{i,lim}$ are the non-linear, $\beta_{i,jnt}$ -dependent joint-stop stiffness and dampening. Equations 27 and 28 define $k_{i,lim}$ and $c_{i,lim}$ to ensure $\mathbf{M}_{i,lim}$ remains continuous at $\beta_{i,jnt} = \beta_{lim}$, where k_0 and c_1 are constants.

$$\mathbf{M}_{i,lim} = \mathbf{R}_{i-1} \begin{pmatrix} -k_{i,lim} (\beta_{i,jnt} - \beta_{lim}) \left(\tilde{\mathbf{z}}_{i-1}^{i-1} \mathbf{R}_i^{i-1} \mathbf{z}_i^i \right) / \sin \beta_{i,jnt} \\ -c_{i,lim} \boldsymbol{\omega}_{i-1,i,\hat{\beta}}^{i-1} \end{pmatrix} \quad (26)$$

$$k_{i,lim}(\beta_{i,jnt}) = \begin{cases} 0, & \beta_{i,jnt} \leq \beta_{lim} \\ k_0, & \beta_{i,jnt} > \beta_{lim} \end{cases} \quad (27)$$

$$c_{i,lim}(\beta_{i,jnt}) = \begin{cases} 0, & \beta_{i,jnt} \leq \beta_{lim} \\ c_1 \cdot (\beta_{i,jnt} - \beta_{lim}), & \beta_{i,jnt} > \beta_{lim} \end{cases} \quad (28)$$

The cable tension $T_{j,k}$ of cable j terminating in segment k will contribute to $\mathbf{M}_{i,act}$ according to Eq. 29. By definition, for the cables terminating in segment 1 at disk 3, the cable tensions in subsegments 4, 5 and 6 are zero, as defined in Eq. 30.

$$\mathbf{M}_{i,act} = \sum_{k=1}^2 \sum_{j=1}^3 (T_{j,k} \mathbf{M}_{i,j,k,cbl}), \quad \mathbf{M}_{i,j,k,cbl} = -\tilde{\mathbf{p}}_{i,j,2H} \hat{\mathbf{p}}_{i,j,2H} \quad (29)$$

$$T_{j,k} = 0, \quad i = \{4,5,6\}, k = 1 \quad (30)$$

2.2.3 Solving the Equations of Motion

The dynamic model presented takes the form of a set of differential-algebraic equations (DAEs): the differential variables are the 12 joint angles (φ_i and θ_i) and the algebraic variables are the four non-zero cable tensions ($T_{j,k}$). If these DAEs are formulated to be linear in the joint accelerations and cable tensions, they can be solved with a conventional ordinary-differential equation (ODE) solver.

However, the cable length constraint defined in Eq. 3 is independent of the joint accelerations. Without loss of generality, this expression may be differentiated twice and utilized as the starting point for a constraint, shown in Eq. 31.

$$\ddot{\delta}_{j,k,des} - \ddot{\delta}_{j,k} = 0 \quad \begin{array}{l} j = \{1,2\} \text{ or } \{2,3\} \text{ or } \{3,1\} \\ k = \{1,2\} \end{array} \quad (31)$$

However, to ensure that the numerical simulation preserves the cable displacement and cable velocity constraints, penalty functions are added to Eq. 31, as shown in Eq. 32, where K_p and K_v are the weights on the cable displacement and velocity errors, respectively. If this expression is integrated without errors in displacement or velocity, it is equivalent to Eq. 31.

$$\ddot{\delta}_{j,k,des} - \ddot{\delta}_{j,k} = -K_p(\delta_{j,k,des} - \delta_{j,k}) - K_v(\dot{\delta}_{j,k,des} - \dot{\delta}_{j,k}) \quad (32)$$

Using Eq. 32 to formulate the cable length constraints, the DAEs take the form shown in Eq. 33. In order to formulate the \mathbf{A} and \mathbf{B} matrices, the inertial loading and cable accelerations should be formulated into $\ddot{\mathbf{q}}$ -dependent terms ($\mathbf{M}_{i,inr,dep} \ddot{\mathbf{q}}$ and $\ddot{\delta}_{j,k,dep} \ddot{\mathbf{q}}$) and $\ddot{\mathbf{q}}$ -independent terms ($\mathbf{M}_{i,inr,ind}$ and $\ddot{\delta}_{j,k,calc,ind}$), as shown in Eq. 34.

$$\begin{bmatrix} \mathbf{A}_{11} & \mathbf{A}_{12} \\ \mathbf{A}_{21} & \mathbf{0} \end{bmatrix} \begin{bmatrix} \ddot{\mathbf{q}} \\ \mathbf{T} \end{bmatrix} = \begin{bmatrix} \mathbf{B}_1 \\ \mathbf{B}_2 \end{bmatrix} \quad (33)$$

$$\mathbf{M}_{i,inr} = \mathbf{M}_{i,inr,dep} \ddot{\mathbf{q}} + \mathbf{M}_{i,inr,ind} \quad (34)$$

$$\ddot{\delta}_{j,k} = \ddot{\delta}_{j,k,dep} \ddot{\mathbf{q}} + \ddot{\delta}_{j,k,ind}$$

The first block row of Eq. 33 (\mathbf{A}_{11} , \mathbf{A}_{12} and \mathbf{B}_1) are the 12 joint equilibrium equations defined in Eq. 1. Formulations for these matrices are provided in Eqs. 35-37, where r is the row index and c is the column index. The indices j and k in Eq. 36 are calculated from the column index—each element of \mathbf{T} corresponds to a specific cable j terminating in segment k .

$$\mathbf{A}_{11}(r,:) = \begin{cases} \rho_r^T \mathbf{M}_{r,inr,dep} & 1 \leq r \leq 6 \\ \gamma_{r-6}^T \mathbf{M}_{r-6,inr,dep} & 7 \leq r \leq 12 \end{cases} \quad (35)$$

$$\mathbf{A}_{12}(r,c) = \begin{cases} -\rho_r^T \mathbf{M}_{r,j,k,cbl} & 1 \leq r \leq 6 \\ -\gamma_{r-6}^T \mathbf{M}_{r-6,j,k,cbl} & 7 \leq r \leq 12 \end{cases}, \quad \{j,k\} = fn(c) \quad (36)$$

$$\mathbf{B}_1(r,1) = \begin{cases} \rho_r^T (\mathbf{M}_{r,el} + \mathbf{M}_{r,grv} - \mathbf{M}_{r,inr,ex}) & 1 \leq r \leq 6 \\ \gamma_{r-6}^T (\mathbf{M}_{r-6,el} + \mathbf{M}_{r-6,grv} - \mathbf{M}_{r-6,inr,ind}) & 7 \leq r \leq 12 \end{cases} \quad (37)$$

The second block row of Eq. 33 (\mathbf{A}_{21} and \mathbf{B}_2) are the 4 cable acceleration equations defined in Eq. 32. Formulations for these matrices are provided in Eqs. 38 and 39. Similar to \mathbf{A}_{12} , the indices j and k in each term are calculated from the row index—each element of \mathbf{T} corresponds to a specific cable j terminating in segment k . However, these mappings are not required to be the same (displacements can be specified for a different set of cables than those tensioned).

$$\mathbf{A}_{21}(r,:) = \ddot{\delta}_{j,k,dep}, \quad [j,k] = fn(r) \quad (38)$$

$$\mathbf{B}_2(r,1) = \begin{pmatrix} \ddot{\delta}_{j,k,des} + K_p(\delta_{j,k,des} - \delta_{j,k}) \\ + K_v(\dot{\delta}_{j,k,des} - \dot{\delta}_{j,k}) - \ddot{\delta}_{j,k,ind} \end{pmatrix}, \quad [j,k] = fn(r) \quad (39)$$

Because the \mathbf{A} matrix is non-singular, the linear system in Eq. 33 may be solved for $\ddot{\mathbf{q}}$ and \mathbf{T} . This provides a means of calculating $\ddot{\mathbf{q}}$ as a function of t , \mathbf{q} and $\dot{\mathbf{q}}$, allowing for implementation of the dynamics solver in a standard MATLAB ordinary differential equation solver (such as ODE45).

A formulation for the statics may also be constructed by ignoring inertial loading. The model's governing equations are defined using Eq. 40, where \mathbf{B} in this case is defined in Eq. 41. Instead of solving a set of ODEs, a set of nonlinear algebraic equations is solved for the vector of 12 joint angles and four non-zero cable tensions.

$$\mathbf{B} = \mathbf{0} \quad (40)$$

$$\mathbf{B}(r,1) = \begin{cases} \rho_r^T (\mathbf{M}_{r,grv} + \mathbf{M}_{r,USDA} + \mathbf{M}_{r,cbl}) & 1 \leq r \leq 6 \\ \gamma_{r-6}^T (\mathbf{M}_{r-6,grv} + \mathbf{M}_{r-6,USDA} + \mathbf{M}_{r-6,cbl}) & 7 \leq r \leq 12 \\ \delta_{j,k,des} - \delta_{j,k} & 13 \leq r \leq 16 \end{cases} \quad (41)$$

3 ELASTICITY OPTIMIZATION

Three of the most critical aspects of the tail's design are the length, mass distribution and tail elasticity. This section will focus on tail elasticity and will consider methods to select springs for a tail of given mass and length. Three approaches will be considered: (1) zero-actuation-configuration, (2) vertical-actuation-minimizing, and (3) horizontal-actuation-minimizing.

These approaches will focus on the selection of extension springs. The compression springs primarily ensure uniformity in yaw-angle actuation—as long as the springs along the tail are the same, this will remain true.

3.1 Considerations for Selecting Extension Springs

A practical concern for the selection of extension springs is ensuring that the subsegment's range of motion can be accommodated by the spring. As discussed in section 2, a mechanical joint stop is incorporated into each subsegment to allow a maximum subsegment bend $\beta_{i,jnt}$ (Eq. 22) of β_{lim} . The pitch and yaw angles associated with the minimum and maximum spring lengths $L_{sp,min}$ and $L_{sp,max}$ are $\varphi_i = \pm \beta_{lim}$ and $\theta_i = 0$ ($L_{sp,min}$ occurs with positive β_{lim}). Using Eq. 10, two conditions for selecting extension springs are: (1) the unloaded spring length $L_{i,spg,0}$ should be less than $L_{sp,min}$, and (2) the

maximum spring extension should be greater than $L_{sp,max} - L_{sp,min}$.

In addition, there are three parameters relevant to the spring's loading associated with the mechanical properties of a spring: the undeformed length, the spring stiffness, and the spring pre-tension. In this analysis, the undeformed spring length will be prescribed, the pretension for the estimated stiffness will be ignored, and the spring stiffnesses will be solved for.

3.2 Simplified Prescribed Configuration Tail Model

For these analyses, a simplified model for the tail will be used to assess the impact of elasticity on the actuation requirements for a prescribed configuration \mathbf{q} . The actuation requirement will be quantified by analyzing the cable tensions $T_{i,A}$ and $T_{i,B}$ in subsegment i cables A and B required to balance the gravitational and USDA loading, shown in Eq. 42.

$$\begin{bmatrix} \rho_i^T \mathbf{M}_{i,A,k,cbl} & \rho_i^T \mathbf{M}_{i,B,k,cbl} \\ \gamma_i^T \mathbf{M}_{i,A,k,cbl} & \gamma_i^T \mathbf{M}_{i,B,k,cbl} \end{bmatrix} \begin{bmatrix} T_{i,A} \\ T_{i,B} \end{bmatrix} = \begin{bmatrix} \rho_i^T (-\mathbf{M}_{i,grv} - \mathbf{M}_{i,USDA}) \\ \gamma_i^T (-\mathbf{M}_{i,grv} - \mathbf{M}_{i,USDA}) \end{bmatrix} \quad (42)$$

3.3 Zero-Actuation-Configuration

The simplest approach to optimize the spring parameters is to select springs that prescribe a straight configuration of the robotic tail in the absence of actuation. This allows for an analytical calculation of the spring stiffnesses, given that $\mathbf{q} = \mathbf{0}$ and $T_{i,A} = T_{i,B} = 0$. By definition, when $\boldsymbol{\theta} = \mathbf{0}$, the yaw moments associated with $\mathbf{M}_{i,grv}$ and $\mathbf{M}_{i,USDA}$ are both zero. Therefore, for each joint i , a stiffness $k_{i,ex}$ may be calculated to satisfy Eq. 43.

$$\rho_i^T \mathbf{M}_{i,USDA} = -\rho_i^T \mathbf{M}_{i,grv} \quad (43)$$

3.4 Vertical-Actuation-Minimizing

For the two additional approaches to selecting spring stiffness, the impact on subsegment cable tensions over a range of configurations will be analyzed. This will provide information on both how the net actuation for a given segment changes along different configuration trajectories, as well as the relative changes in actuation requirements between subsegments within a given segment.

For the vertical-actuation case, the tail will move through a prescribed set of configurations in the vertical x - z plane between the tail's extreme configurations from $\varphi_i = -\beta_{lim}$ to $\varphi_i = \beta_{lim}$ as the parameter ζ varies from 0 to 1. As shown in Ex. 44, linear interpolation is used to create this vertical trajectory for φ_i while θ_i is held constant at zero.

$$\varphi_i(\zeta) = -\beta_{lim} + 2\beta_{lim}\zeta, \quad \theta_i = 0 \quad (44)$$

Like section 3.3, motion restricted to the vertical plane inherently satisfies the yaw-joint equilibrium equations, leading to an algebraic constraint between the two cable tensions. In this analysis, the actuation cabling will be arranged so that in the vertical actuation case, either only cable 1 is in tension ($T_{i,A} = T_{i,vrt}$, $T_{i,B} = 0$) or cables 2 and 3 are both in tension with equal magnitude ($T_{i,A} = T_{i,B} = 0.5T_{i,vrt}$). This results in a simplification

of Eq. 42 into Eq. 45 for this case. Furthermore, the subsegment actuation requirement may be characterized by $T_{i,vrt}$.

$$\begin{bmatrix} \rho_i^T \mathbf{M}_{i,A,k,cbl} & \rho_i^T \mathbf{M}_{i,B,k,cbl} \end{bmatrix} \begin{bmatrix} T_{i,A} \\ T_{i,B} \end{bmatrix} = \rho_i^T (-\mathbf{M}_{i,grv} - \mathbf{M}_{i,USDA}) \quad (45)$$

Equations 46 and 47 define the parameters $T_{l,mag,vrt}$ and $T_{l,diff,vrt}$ used to parameterize the segment l actuation magnitude ($T_{l,mag,vrt}$) and relative actuation requirements ($T_{l,diff,vrt}$) for subsegments $3l-2$, $3l-1$ and $3l$. These parameters provide a closed-form calculation that measures the variation between the prescribed kinematic configuration and the actual equilibrium configuration (subject to the same cable displacement inputs for the kinematic and static models). Equations 46 and 47 define $T_{l,mag,vrt}$ and $T_{l,diff,vrt}$ over the domain of ζ , which parameterizes the tail trajectory.

$$T_{l,mag,vrt} = \sqrt{\frac{1}{3} \int_0^1 (T_{3l-2,vrt}^2 + T_{3l-1,vrt}^2 + T_{3l,vrt}^2) d\zeta} \quad (46)$$

$$T_{l,diff,vrt} = \sqrt{\frac{1}{3} \int_0^1 \left((T_{3l-1,vrt} - T_{3l-2,vrt})^2 + (T_{3l,vrt} - T_{3l-1,vrt})^2 + (T_{3l,vrt} - T_{3l-2,vrt})^2 \right) d\zeta} \quad (47)$$

For a given segment l , there are three spring stiffnesses to be optimized: $k_{3l-2,ex}$, $k_{3l-1,ex}$ and $k_{3l,ex}$, which may be represented in vector form as $\mathbf{k}_{(3l-2):(3l),ex}$. Using $T_{l,mag,vrt}$ and $T_{l,diff,vrt}$, both of which depend on $\mathbf{k}_{(3l-2):(3l),ex}$, an optimization can be constructed to minimize the weighted sum of these parameters over the three positive real-valued spring stiffnesses $\mathbf{k}_{(3l-2):(3l),ex}$, as shown in Eq. 48. The weights $w_{k,1}$ and $w_{k,2}$ are chosen to balance the relative importance of the magnitude and difference conditions.

$$\min_{\mathbf{k}_{(3k-2):(3k),ex} \in (\mathbf{R}^+)^3} (w_{k,1} T_{k,mag,vrt} + w_{k,2} T_{k,diff,vrt}) \quad (48)$$

3.5 Horizontal-Actuation-Minimizing

The parameterized horizontal tail trajectory is defined in Eq. 49. Unlike the vertical plane motion, both the pitch- and yaw-joint equilibrium conditions defined in Eq. 42 will be utilized to calculate the two subsegment i cable tensions $T_{i,A}$ and $T_{i,B}$. For these simulations, A will remain 1, and B will vary between 2 and 3, depending on the direction of bending. Furthermore, because of the mechanism's symmetry, only the angles in the range $0 \leq \theta_i \leq \beta_{lim}$ are considered.

$$\varphi_i = 0, \quad \theta_i = \beta_{lim}\zeta \quad (49)$$

Parameters $T_{l,j,mag}$ and $T_{l,j,diff}$ for the magnitude and difference conditions for cable j in segment l are defined in Eqs. 50-51. An optimization similar to Eq. 48 is constructed in Eq. 52 using the four parameters for a given segment k .

$$T_{l,j,mag,hrz} = \sqrt{\frac{1}{3} \int_0^1 (T_{3l-2,j,hrz}^2 + T_{3l-1,j,hrz}^2 + T_{3l,j,hrz}^2) d\zeta} \quad (50)$$

$$T_{l,j,diff,hrz} = \sqrt{\frac{1}{3} \int_0^1 \left(\begin{aligned} &(T_{3l-1,j,hrz} - T_{3l-2,j,hrz})^2 \\ &+ (T_{3l,j,hrz} - T_{3l-1,j,hrz})^2 \\ &+ (T_{3l,j,hrz} - T_{3l-2,j,hrz})^2 \end{aligned} \right) d\zeta} \quad (51)$$

$$\min \sum_{j=A,B} (w_{l,j,1} T_{l,j,mag,hrz} + w_{l,j,2} T_{l,j,diff,hrz}) \quad (52)$$

$$\mathbf{k}_{(3l-2)(3l),ex} \in (\mathbf{R}^+)^3$$

4 RESULTS

This section utilizes the mechanical models (static and dynamic) and spring optimization cases to analyze a robotic tail structure. Simulation properties are defined in section 4.1, and the optimal spring stiffnesses are analyzed and calculated in section 4.2. Then, in sections 4.3 and 4.4, the quasi-static and dynamic trajectories of the tails are compared to analyze the impact inertial loading has on the tail performance.

4.1 Simulation Properties

Table 1 defines various properties of the robotic tail under consideration extracted from a preliminary CAD design of the tail. These properties are either themselves utilized in the model definitions of previous sections, or will be utilized in this section to define additional properties.

The body-frame extension spring anchor positions $\mathbf{p}_{1,D2S}^{i-1}$ are defined in Eq. 53. The $\mathbf{p}_{1,D2S}^{i-1}$ z-coordinate is chosen such that the ‘base’ spring anchor vertically aligns with the universal joint center; the $\mathbf{p}_{1,D2S}^{i-1}$ x-coordinate is adjustable. The x-coordinates are different to accommodate the spring anchors of both joints $i-1$ and i on disk i . For these simulations, $L_{i,spg,0}$ and $F_{i,spg,0}$ are equal for each joint i to allow the spring stiffness to quantify the different extension spring loading requirements.

$$\mathbf{p}_{1,D2S}^{i-1} = [30 \ 0 \ 5]^T \text{ mm}, \quad \mathbf{p}_{2,D2S}^{i-1} = [20 \ 0 \ -10]^T \text{ mm} \quad (53)$$

A formulation for the $k_{i,cp}$ of a helical compression spring is defined in Eq. 54, where E_{ex} and G_{ex} are the spring’s Young’s and shear moduli, I_{ex} is the spring wire’s cross-sectional second-moment of area, n_{ex} is the number of turns of the coil bending and r_{ex} is the spring’s helical radius [18].

$$k_{i,cp} = 2E_{ex}G_{ex}I_{ex}/\pi n_{ex}r_{ex}(E_{ex} + 2G_{ex}) \quad (54)$$

The three cable actuation routing holes are positioned at radius r_{hl} and spaced 120° apart. The cable 1 routing hole is defined to intersect the $-x$ -axis in the local frame, leading to the

Table 1. Tail properties.

L_{J2C}	72 mm	L_{J2D}	75 mm	L_{J2J}	80 mm
m_i	75 g	$F_{i,spg,0}$	0 N	$L_{H2H,0}$	38.1 mm
$I_{j,xx}^j$	43.021e-12 kg-m ²	$I_{j,yy}^j$	44.337e-12 kg-m ²	$I_{j,zz}^j$	28.548e-12 kg-m ²
E_{ex}	210e9 Pa	G_{ex}	80e9 Pa	r_{ex}	8.06 mm
n_{ex}	2.7	I_{ex}	2.13e-12 m ⁴	$c_{i,dmp}$	0.1 N-m-s/rad
r_{hl}	32.5 mm				

formulation for $\mathbf{p}_{j,hl}^i$ in Eq. 55.

$$\mathbf{p}_{j,hl}^i = r_{hl} [c_\psi \ s_\psi \ 0]^T, \quad \psi = 120^\circ(j-1) + 180^\circ \quad (55)$$

4.2 Elasticity Optimization Results

The three approaches for generating extension spring stiffnesses were implemented in MATLAB and the results are shown in Table 2. The zero-actuation-configuration solver (section 5.3) utilized the ‘fsolve’ function to calculate the six stiffnesses required to solve the six scalar equations defined in Eq. 43. The vertical- and horizontal-actuation-minimizing optimizations are solved in two ways: an unconstrained optimization (using ‘fminunc’) without limits on the spring stiffnesses, and a constrained optimization (using ‘fmincon’) with a lower bound on each spring stiffness ($k_{i,ex} > 0$). The unconstrained optimizations illustrate the ‘optimal’ spring configuration, in which a negative stiffness denotes the extension spring should be below the universal joint, instead of above.

The stiffnesses for the zero-actuation-configuration and vertical-actuation-minimizing approaches represent two extremes, and the horizontal-actuation-minimizing strikes a balance between the two. As a result, the stiffnesses associated with the horizontal-actuation-minimizing will be used in subsequent simulations.

4.3 Static Tail Analysis

First, the configurations of the unloaded tail and the tail when cable displacements are prescribed as zero are shown in Fig. 4. Because the horizontal-actuation-minimizing set of spring stiffnesses were chosen, the unloaded tail configuration is not straight, but the actuation requirements to ‘straighten’ the tail are minimal (for the zero-displacement in Fig. 4(b), 11.15 N are required in segment 1 cables 2 and 3 and 2.33 N are required in segment 2 cables 2 and 3).

For the simulations in sections 4.3 and 4.4, a set of prescribed cable trajectories $\delta_{j,k}$ are generated from a ‘desired’ joint angle trajectory, both shown in Fig. 5.

As described in section 2.2.3, the static model is solved as a set of 16 nonlinear equations for the 16 coordinates (12 joint angles and 4 cable tensions); for the static tail trajectory, the prescribed cable trajectories are calculated at a set of prescribed timesteps, and the static model is solved at each timestep. To speed-up calculations, the previous time step’s solution is used as the initial guess for the current time step, and an estimate for cable tensions is used at the first time step.

Table 2. Calculated stiffnesses (units: N/m)

Joint	Zero-Act.	Horizontal		Vertical	
		Uncon.	Con.	Uncon.	Con.
1	1463.8	700.8	700.8	486.4	591.1
2	1040.4	527.7	527.7	119.9	224.6
3	688.8	342.4	342.4	-123.3	0
4	409.0	131.8	279.6	-248.2	4.3
5	200.9	-32.8	115.1	-286.1	0
6	64.6	-156.9	0	-279.8	0

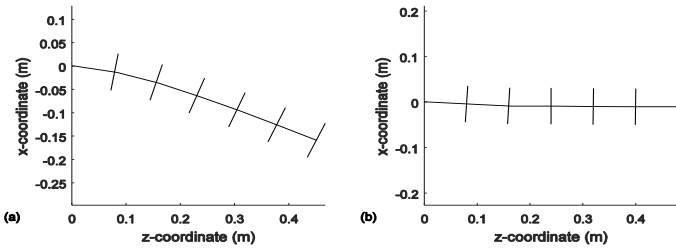


Figure 4. (a) Unloaded tail configuration (no applied displacements or cable forces), (b) Tail configuration with prescribed zero displacement.

Figure 6 illustrates the static trajectories for the φ - and θ -joint angles (Figs. 6(a) and 6(b), respectively) compared to the kinematic trajectories in Fig. 5(a). There is a strong correlation between the kinematic and static θ -joint trajectories, but there is variation in the φ -joint trajectories, particularly in segment 1. This is due to the variation in gravitational loading along the segment as the segment bends. The cable displacement constraints effectively set the sum of the pitch angles along the segment, but do not enforce that the individual joint angles be equal, as shown. Trigonometric nonlinearities also lead to the sum of these angles to be nonzero, despite the fact that the sum of the desired joint angles is zero in the pitch direction.

Figure 7 illustrates the cable tension trajectories during the static tail trajectory. Due to the symmetry of the mechanism across the x-z plane, the tension profiles are symmetric across the 0.25 s vertical line, with the tensions in cables 2 and 3 switched across this boundary. As the central compression springs are the same for all six joints, the segment 2 cable tensions carry most of the load in the six subsegments, as the tensions from the segment 2 cables are applied to segment 1 as the cables route through this segment. To reduce the static

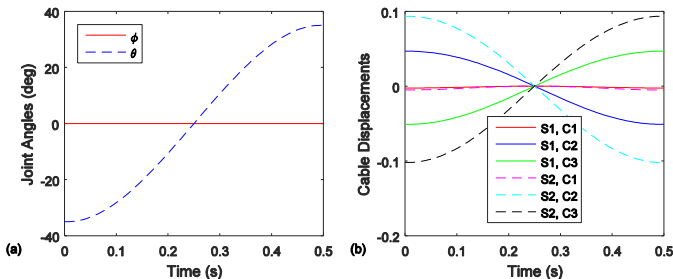


Figure 5. (a) 'Desired' kinematic USRT joint angle trajectory. (b) Prescribed cable displacement trajectories calculated from desired joint angle trajectories.

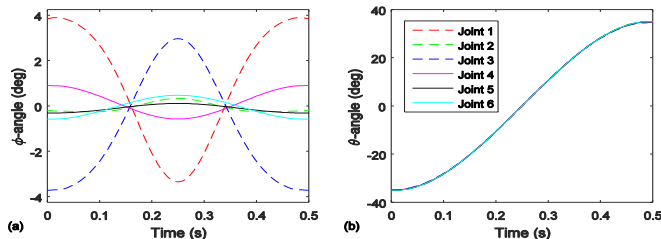


Figure 6. Static joint angle trajectories (a) φ -joints, (b) θ -joints.

actuation requirements of the segment 2 motors, the stiffness of the compression springs in segment 2 can be reduced. If the spring stiffnesses in segment 1 are not also reduced, this will increase the static loading requirement of segment 1.

4.4 Dynamic Tail Trajectories

Figures 8 and 9 illustrate the dynamic trajectories for the φ -joint (Fig. 8) and θ -joint (Fig. 9). A significant variation in the dynamic θ -joint trajectories is seen in Fig. 9 in comparison to the static θ -joint trajectories in Fig. 6(b). This variation is primarily due to the difference in the effective inertia at each joint. For example, when the tail is fully extended (all joint angles equal zero), the x-axis inertia (I_{xx}) at joint 1 is 0.0420 kg-m², whereas for joint 3 the inertia is 0.0136 kg-m². As a result, given the same cable tension applied in each segment (assuming the segments start in the same initial configuration), joint 3 will show greater angular acceleration than joint 1.

As the trajectory evolves, the elastic springs help to balance the acceleration between the joints, but because the compression springs have equal stiffness, this requires disparity in the segment's joint angles. Furthermore, as the joint angles change, the transmission efficiency between the cable and joint changes, also affecting the relative actuation loading. Once an

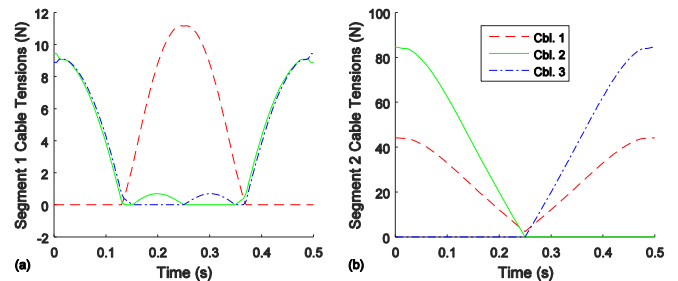


Figure 7. Static trajectory cable tensions.

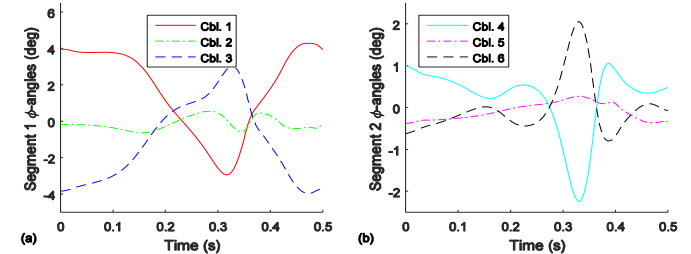


Figure 8. φ -joint dynamic trajectories: (a) segment 1, (b) segment 2.

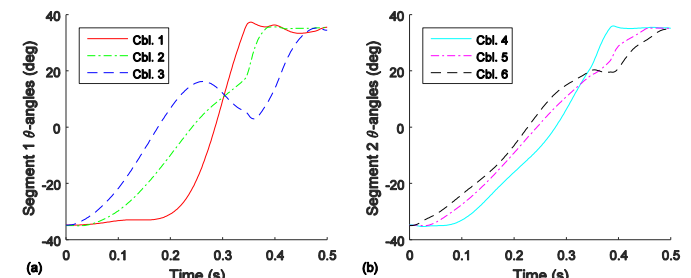


Figure 9. θ -joint dynamic trajectories (a) segment 1, (b) segment 2.

individual universal joint reaches its joint stop, the modeled nonlinear spring will prevent further bending in that subsegment, causing the remaining segments to bend further.

Figure 10 illustrates the cable tensions during the dynamic trajectory. Like the joint angle trajectories, there are significant variations compared to the static cable tensions for the same trajectory in Fig. 7. For the segment 2 tensions in Fig. 10(b), although the topology of the figure is similar, the time at which the cable tension shifts from cable 2 to cable three has shifted by 0.05 sec (a 20% shift relative to the static value). The compression spring loading is used to overcome the inertial loading by reducing the cable tension constraining the bent spring. However, once zero tension is reached in cables 1 and 2, cables 1 and 3 are required to ‘pull’ the segment toward the desired final configuration, overcoming the tension

For the segment 1 tensions in Fig. 10(a), the topology changed. In Fig. 7(a), the cable tensions primarily acted against pitch angle variations, given the equal cable tensions in cable 2 and 3 in the initial and final sections of the trajectory, and the dominant tension in cable 1 in the middle section. However, in Fig. 10(b), the cable tensions must contribute significantly to overcoming the increased segment 1 joint inertias compared to segment 2 as discussed above. Therefore, to accelerate the segment, cables 1 and 3 are tensioned in the first section of the trajectory, and to decelerate the segment cables 1 and 2 are tensioned in the second section of the trajectory. In addition, the peaks present in the force loading profile correlate to points at which the joint limit is hit in Fig. 9(a).

5 CONCLUSION

This paper has focused on the design concept and associated mechanical model of a novel robotic tail composed of a serial chain of universal-joints, actuated by cables and supported by elastic springs along the structure. A dynamic model in the form of coupled differential-algebraic equations was derived, along with a static model composed of nonlinear algebraic equations. Three approaches for optimizing spring stiffnesses were presented, along with results comparing the kinematic, static and dynamic trajectories (joint angle and tension) associated with the prescribed cable displacements.

The robotic system described in this work will be used to study the effectiveness of a robotic tail in maneuvering and stabilizing mobile robots, particularly legged robots. Future work will focus on the integration of a USRT for experimental

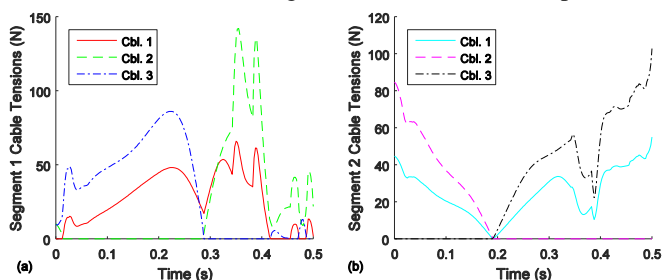


Figure 10. Dynamic cable trajectories: (a) segment 1, (b) segment 2.

validation of the dynamics model and the proposed tail functionalities. In parallel with this experimental work, methods of sensing, state estimation and tail control for the robotic tail will also be studied and implemented. Planned improvements for the USRT dynamic model include accounting for friction losses along the actuation cabling and considering the other mechanical effects that may be introduced due to additional structures for sensing.

ACKNOWLEDGMENTS

This material is based upon work supported by the National Science Foundation under Grant No. 1557312.

REFERENCES

- [1] Rone, W. S., and Ben-Tzvi, P., 2016, “Dynamic Modeling and Simulation of a Yaw-Angle Quadruped Maneuvering with a Robotic Tail,” *J. Dyn. Syst. Meas. Control.*, **138**(8), p. 084502: 1-7.
- [2] Berenguer, F. J., and Monasterio-Huelin, F. M., 2008, “Zappa, a Quasi-Passive Biped Walking Robot With a Tail: Modeling, Behavior, and Kinematic Estimation Using Accelerometers,” *IEEE Trans. Ind. Electron.*, **55**(9), pp. 3281–3289.
- [3] Briggs, R., Lee, J., Haberland, M., and Kim, S., 2012, “Tails in Biomimetic Design: Analysis, Simulation, and Experiment,” *IEEE/RSJ International Conference on Intelligent Robots and Systems*, Vilamoura, Algarve, Portugal, pp. 1473–1480.
- [4] Casarez, C., Penskiy, I., and Bergbreiter, S., 2013, “Using an Inertial Tail for Rapid Turns on a Miniature Legged Robot,” *IEEE International Conference on Robotics and Automation*, IEEE, Karlsruhe, Germany, pp. 5469–5474.
- [5] Ikeda, F., and Toyama, S., 2015, “A Proposal of Right and Left Turning Mechanism for Quasi-Passive Walking Robot,” *IEEE International Conference on Advanced Robotics and Intelligent Systems*, Taipei, Taiwan.
- [6] Chang-Siu, E., Libby, T., Tomizuka, M., and Full, R. J., 2011, “A Lizard-inspired Active Tail Enables Rapid Maneuvers and Dynamic Stabilization in a Terrestrial Robot,” *2011 IEEE/RSJ International Conference on Intelligent Robots and Systems*, San Francisco, CA, pp. 1887–1894.
- [7] Robinson, G., and Davies, J. B. C., 1999, “Continuum Robots - A State of the Art,” *IEEE International Conference on Robotics and Automation*, Detroit MI, pp. 2849–2854.
- [8] Rone, W. S., and Ben-Tzvi, P., 2014, “Continuum Robot Dynamics Utilizing the Principle of Virtual Power,” *IEEE Trans. Robot.*, **30**(1), pp. 275–287.
- [9] Wei, W., Xu, K., and Simaan, N., 2006, “A Compact Two-Armed Slave Manipulator for Minimally Invasive Surgery of the Throat,” *IEEE/RAS-EMBS International Conference on Biomedical Robotics and Biomechatronics*, Pisa, Italy, pp. 769–774.
- [10] McMahan, W., Jones, B. A., and Walker, I. D., 2005, “Design and Implementation of a Multi-section Continuum Robot: Air-Octor,” *IEEE/RSJ International Conference on Intelligent Robots and Systems*, Alberta, CA, pp. 2578–2585.
- [11] Wright, C., Buchan, A., Brown, B., Geist, J., Schwerin, M., Rollinson, D., Tesch, M., and Choset, H., 2012, “Design and Architecture of the Unified Modular Snake Robot,” *IEEE International Conference on Robotics and Automation*, St. Paul, MN, pp. 4347–4354.
- [12] OC-Robotics, 2015, “Snake-Arm Robots” [Online]. Available: <http://www.ocrobotics.com/technology--innovation/>. [Accessed:]

20-Jan-2015].

- [13] McMahan, W., Chitrakaran, V., Csencsits, M. A., Dawson, D. M., Walker, I. D., Jones, B. A., Pritts, M., Dienno, D., Grissom, M., and Rahn, C. D., 2006, "Field Trials and Testing of the OctArm Continuum Manipulator," IEEE International Conference on Robotics and Automation, Orlando, FL, pp. 2336–2341.
- [14] Hannan, M. W., and Walker, I. D., 2003, "Kinematics and the Implementation of an Elephant's Trunk Manipulator and Other Continuum Style Robots," J. Robot. Syst., **20**(2), pp. 45–63.
- [15] Saab, W., Rone, W. S., Kumar, A., and Ben-Tzvi, P., "Design and Integration of a Novel Spatial Articulated Robotic Tail," IEEE Trans. Robot., Under Review.
- [16] Saab, W., and Ben-Tzvi, P., 2016, "Design and Analysis of a Discrete Modular Serpentine Tail," ASME International Design Engineering Technical Conference & Computers and Information in Engineering Conference, ASME, Charlotte, NC, p. 59387: 1-8.
- [17] Rone, W. S., and Ben-Tzvi, P., 2015, "Static Modeling of a Multi-Segment Serpentine Robotic Tail," ASME International Design Engineering Technical Conference & Computers and Information in Engineering Conference, Boston, MA.
- [18] Wahl, A. M., 1944, Mechanical Springs, Penton Publishing Company, Cleveland, Ohio.